Magnetic anisotropy and the phase diagram of chiral $MnSb_2O_6$

J. Werner, C. Koo, and R. Klingeler*
Kirchhoff Institute of Physics, Heidelberg University, INF 227, D-69120 Heidelberg, Germany
and Centre for Advanced Materials, Heidelberg University, INF 225, 69120 Heidelberg, Germany

A. N. Vasiliev
Physics Faculty, M.V. Lomonosov Moscow State University, Moscow 119991, Russia;
Theoretical Physics and Applied Mathematics Department, Ural Federal University, 620002 Ekaterinburg, Russia;
and National University of Science and Technology "MISiS", Moscow 119049, Russia

Y. A. Ovchenkov, A. S. Polovkova, G. V. Raganyan, and E. A. Zvereva
Physics Faculty, M.V. Lomonosov Moscow State University, Moscow 119991, Russia
(Received 6 June 2016; revised manuscript received 9 August 2016; published 6 September 2016)

The magnetic phase diagram and low-energy magnon excitations of structurally and magnetically chiral $MnSb_2O_6$ are reported. The specific heat and the static magnetization are investigated in magnetic fields up to 9 and 30 T, respectively, while the dynamic magnetic properties are probed by X-band as well as tunable high-frequency electron spin-resonance spectroscopy. Below $T_N = 11.5$ K, we observe antiferromagnetic resonance modes which imply small but finite planar anisotropy showing up in a zero-field splitting of 20 GHz. The data are well described by means of an easy-plane two-sublattice model with the anisotropy field $B_A = 0.02$ T. The exchange field $B_E = 13$ T is obtained from the saturation field derived from the pulsed-field magnetization. A crucial role of the small anisotropy for the spin structure is reflected by competing antiferromagnetic phases appearing, at $T = 2$ K, in small magnetic fields at $B_{C1} \approx 0.5$ T and $B_{C2} = 0.9$ T. We discuss the results in terms of spin reorientation and of small magnetic fields favoring helical spin structure over the cycloidal ground state which, at $B = 0$, is stabilized by the planar anisotropy. Above T_N, short-range magnetic correlations up to $\gtrsim$60 K and magnetic entropy changes well above T_N reflect the frustrated triangular arrangement of Mn^{2+} ions in $MnSb_2O_6$.

DOI: 10.1103/PhysRevB.94.104408

I. INTRODUCTION

Frustrated or low-dimensional magnetic materials exhibiting low-energy magnetic excitations in which complex magnetic order is coupled to structure and dielectric properties are promising candidates for multiferroic properties [1–4]. On the microscopic point of view, magnetic anisotropy has been proven an essential ingredient in a multitude of systems with significant magnet-electric coupling. In $BiFeO_3$, where both magnetic ordering at $T_N = 650$ K and ferroelectricity at $T_C = 1100$ K appear well above room temperature [5], anisotropy is crucial for stabilizing the actual cycloidal spin configuration [6]. This also holds for $MnSb_2O_6$, a structurally and magnetically chiral system which is predicted to be multiferroic with a unique ferroelectric switching mechanism based on its corotating cycloidal magnetic structure [7]. Despite its relevance, the size of magnetic anisotropy has not been experimentally determined yet.

$MnSb_2O_6$ crystallizes in the trigonal space group P321 and exhibits structural chirality [7,8]. In the layered structure, triples of MnO_6 distorted octahedra connected by SbO_6 octahedra, thereby forming isolated triangles of magnetic Mn^{2+} ions. Below $T_N = 12.5$ K, incommensurate long-range antiferromagnetic order evolves with the spin structure being based on corotating cycloids [8]. The experimentally observed magnetic structure can be derived from *ab initio* density functional theory (DFT) calculations with magnetic anisotropy playing a crucial role for establishing the ground state [7]. We hence present a detailed study of the static and dynamic magnetic properties of $MnSb_2O_6$ with particular emphasis on magnetic anisotropy. Experimentally, we apply specific heat and magnetization measurements in static and pulsed magnetic field as well as X-band (LF-ESR) and tunable high-frequency/high-field electron spins resonance (HF-ESR) studies. The magnetic phase diagram of $MnSb_2O_6$ shows three antiferromagnetic phases, two of which are limited to small magnetic fields $\simeq$1 T, i.e., well below the saturation field of about 26 T. The antiferromagnetic resonance (AFMR) modes probed by HF-ESR imply an easy plane-type behavior and a zero-field splitting of approximately 20 GHz. Broadening of the HF-ESR resonances and magnetic entropy changes well above T_N suggest short-range AFM fluctuations up to $\gtrsim$60 K.

II. EXPERIMENTAL

Polycrystalline $MnSb_2O_6$ was prepared by conventional solid-state synthesis as reported elsewhere [9]. Phase purity was confirmed by x-ray diffraction. Refined hexagonal lattice parameters [$a = 8.8035(17)$, $c = 4.7266(12)$ Å] are in a good agreement with the literature [8,10].

HF-ESR measurements were carried out using a phase-sensitive millimeter-wave vector network analyzer (MVNA) from AB Millimetré covering the frequency range from 30 to 1000 GHz [11]. For each frequency range (Q, L, W band, etc.), different sets of Schottky diode systems were used. Experiments were performed in a 18-T superconducting magnet with temperature control sensors in both probe and

*klingeler@kip.uni-hd.de

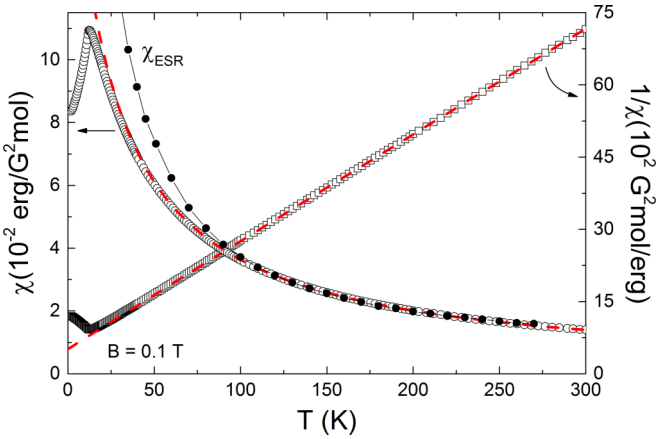

FIG. 1. Static magnetic susceptibility $\chi = M/B$ of $MnSb_2O_6$, at B = 0.1 T, and χ_{ESR} obtained from doubly integrating the LF-ESR spectra vs temperature. The dashed lines display a Curie-Weiss approximation to the high-temperature regime with $p_{eff} = 5.93$ μ_B and $\Theta = -23$ K (see the text).

sample space. $MnSb_2O_6$ loose powder was placed in the sample space of the cylindrical waveguide probe without any glue or grease. LF-ESR studies were carried out in an X-band ESR spectrometer CMS 8400 (ADANI) ($f \approx 9.4$ GHz, $B \leqslant 0.7$ T) with a BDPA (a,g-bisdiphenyline-b-phenylallyl) reference sample which labels $g = 2.00359$. Static magnetic properties were measured with a Quantum Design MPMS XL-5 superconducting quantum interference device magnetometer and a Quantum Design PPMS-9 system, respectively. The latter system has been applied to obtain the specific heat, too. Magnetization studies in pulsed magnetic fields up to 30 T were performed in a magnet with a rise time of about 8 ms.

III. STATIC MAGNETIZATION AND MAGNETIC PHASE DIAGRAM

The static magnetic susceptibility $\chi = M/B$ of $MnSb_2O_6$ (Fig. 1) confirms long-range antiferromagnetic order below $T_N = 11.5(5)$ K. The onset of long-range magnetic order is particularly evident in the magnetic specific heat $c_p^{magn} = \partial(\chi T)/\partial T$ which exhibits a pronounced λ-like anomaly at T_N [Fig. 3(a)] [12]. Note that in Ref. [8] a slightly different value of T_N was derived from the maximum in χ. In the high-temperature regime χ obeys a Curie-Weiss law $\chi_{cw} = \chi_0 + (N_A p_{eff}^2)/[3k_B(T + \Theta)]$, with χ_0 being a temperature-independent contribution, N_A the Avogadro number, p_{eff} the effective magnetic moment, k_B the Boltzmann constant, and Θ the Weiss temperature. Fitting the data by means of the Curie-Weiss equation yields $p_{eff} = 5.93(2)$ μ_B, $\Theta = -23(1)$ K, and $\chi_0 = 2(1) \times 10^{-4}$ erg/(G^2 mol). The obtained effective moment nearly perfectly agrees with what is expected for high-spin Mn^{2+} ions with $S = 5/2$ and $g = 1.995$, the latter found in our ESR measurements (see below). Below $T \approx 55$ K, the mean-field description starts to deviate from the experimental data indicating the onset of antiferromagnetic fluctuations, while long-range antiferromagnetic spin order evolves at T_N.

The field dependence of the magnetization $M(B)$ in Fig. 2 corroborates antiferromagnetic behavior at low temperatures.

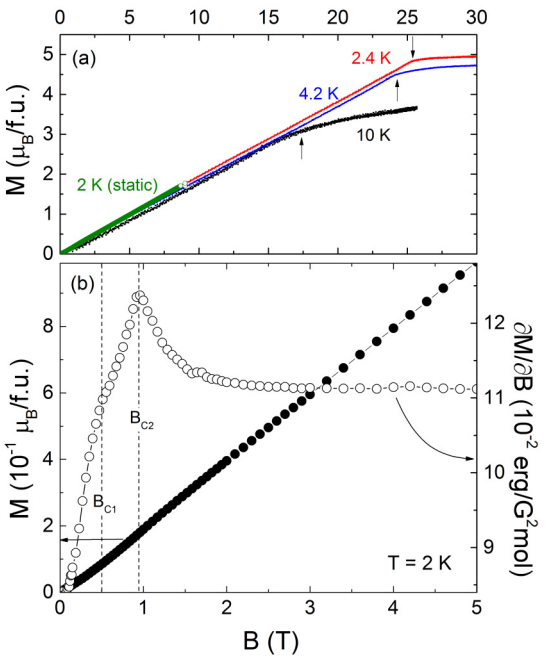

FIG. 2. (a) Pulsed field magnetization vs external field at $T = 2.4$, 4.2, and 10 K are shown together with data (open circles) obtained in quasistatic field. The arrows mark the saturation fields B_C, viz., the antiferromagnetic phase boundary. (b) Magnetization M and its derivative $\partial M/\partial B$ of $MnSb_2O_6$ vs external magnetic field, at $T = 2$ K. The dashed lines indicate two anomalies at B_{C1} and B_{C2}.

For $B > 2$ T, there is a linear field dependence of M. At high fields, right bending of the magnetization curves obtained in pulsed magnetic fields up to $B = 30$ T shown in Fig. 2(a) indicates the antiferromagnetic phase boundary (cf. Fig. 4). At $T = 2.4$ K, the associated critical field is $B_C = 25.3$ T and the observed value $M(T = 2.4\,\text{K}, B = 25.3\,\text{T}) = 4.9$ μ_B/f.u. is close to the theoretical saturation magnetization. Extrapolating the data suggests the saturation field at zero temperature of $B_C \approx 26$ T. At small magnetic fields, the M versus B curve is slightly left-bending which is often associated to magnetic anisotropy. In contrast to a typical spin floplike behavior, in $MnSb_2O_6$ left-bending is associated with two separated anomalies at $B_{C1} \approx 0.5$ T and $B_{C2} = 0.9$ T, at $T = 2$ K. As seen in Fig. 3(b), both anomalies are restricted to the long-range antiferromagnetic ordered phase. Upon heating from $T = 2$ K, B_{C1} is essentially constant while B_{C2} clearly increases and significantly broadens. E.g., at 9 K, B_{C2} amounts to 1.5 T. The field dependence of T_N is derived from the specific heat shown in Figs. 3 and 5. At low temperatures, the data clearly deviate from the Curie-Weiss behavior but obey the mean-field description at $T \gtrsim 55$ K.

The observed positive slope of the phase boundary $B_{C2}(T)$ agrees to the associated increase in magnetization. Quantitatively, the slope of the phase boundary is associated with the ratio of the entropy changes ΔS and the magnetization changes ΔM at the phase transition according to $dB_C/dT = -\Delta S/\Delta M$ (Clausius-Clapeyron relation) [13]. Applying the experimental results $dB_{C2}/dT \approx 6 \times 10^{-2}$ T/K and $\Delta M_{C2} = 0.013$ μ_B/f.u. yields entropy changes of $\Delta S_{C2} \approx 4$mJ/(mol K)

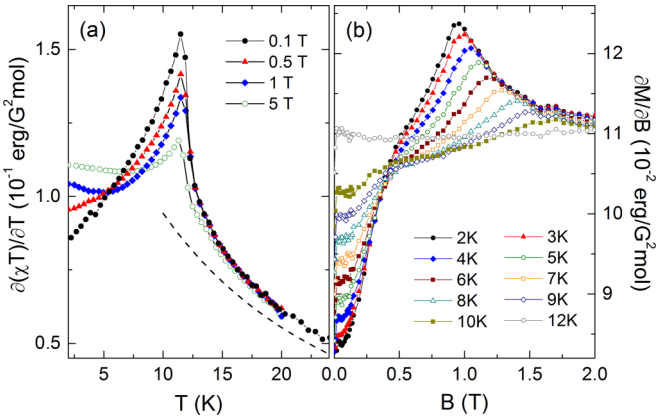

FIG. 3. (a) Magnetic specific heat $c_p^{magn} = \partial(\chi T)/\partial T$ as derived from the static susceptibility, indicating a λ-like anomaly at $T_N = 12$ K, at different external fields. The dashed line shows the Curie-Weiss behavior $\partial(\chi_{cw}T)/\partial T$. (b) Derivative $\partial M/\partial B$ of the magnetization vs external magnetic field, at different temperatures.

associated with B_{C2}, i.e., with changing from AF2 → AF3 (see the phase diagram in Fig. 4).

Specific-heat data presented in Fig. 5 confirm negligible entropy changes at $B_{C2}(T < 7$ K). The data show λ-like anomalies at $T_N(B)$ in good agreement with the magnetization data. The respective values for T_N obtained at $B = 0,3,6$, and 9 T (not all data are shown in Fig. 5) are displayed in Fig. 4. In addition to the anomalies at T_N, there is a hump at $T^* \approx 4$ K which is not affected by magnetic fields up to 9 T. It is presumingly not associated to a nuclear Schottky anomaly. At temperatures around T_N, there are clear entropy changes associated with a suppression of long-range antiferromagnetic order. In addition, there is a field induced increase of specific heat at $T > 16$ K, i.e., $c_p(B = 9$ T$) > c_p(B = 0$ T). Quantitatively, $c_p(T = 25$ K) increases by about 0.5 J/(mol K) upon application of $B = 9$ T. This behavior may

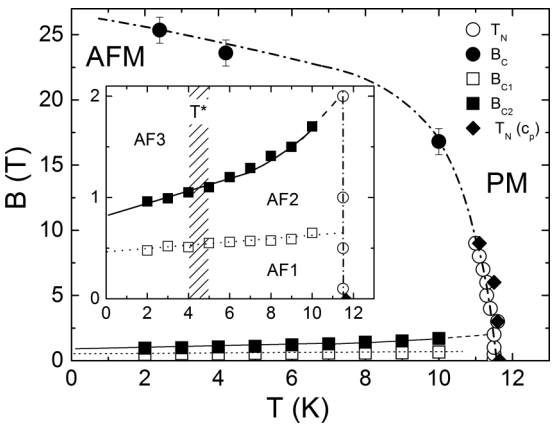

FIG. 4. Magnetic phase diagram of $MnSb_2O_6$. The dot-dashed line shows the magnetic field dependence of T_N as derived from M and c_p vs T measurements at different magnetic fields [cf. Figs. 3(a) and 5]. The dotted and straight lines refer to B_{C1} and B_{C2}, respectively, taken from M vs B [cf. Fig. 3(b) and Fig. 2]. AF1, AF2, and AF3 label the different antiferromagnetic phases, and PM labels the paramagnetic one. The shaded area reflects the humplike feature observed in the specific-heat data at T^*.

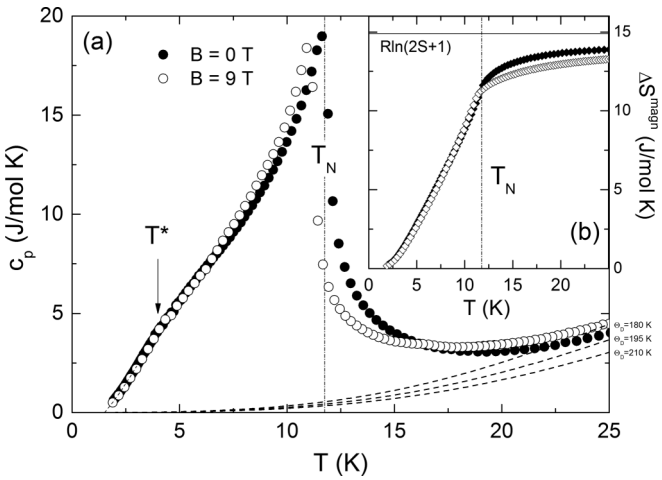

FIG. 5. (a) Specific heat c_p and (b) magnetic entropy changes of $MnSb_2O_6$. The dashed lines show the phonon contribution c_p^{ph} according to $\Theta_D = 180$, 195, and 210 K, respectively. Dash-dotted lines show T_N at $B = 0$ and the dotted line extrapolates c_p to low temperatures. Entropy changes in (b) have been calculated by integrating $(c_p\text{-}c_p^{ph})/T$.

suggest the presence of competing ferromagnetic coupling (cf. [14]) which would qualitatively disagree with the DFT results in Ref. [7], i.e., the presence of antiferromagnetic exchange interactions only.

As illustrated in Fig. 5, the phonon contribution is negligible below 5 K. This is illustrated in Fig. 5 by dashed lines which show the phonon specific heat for $\Theta_D = 180$, 195, and 210 K, respectively. While $c_p^{ph}(\Theta_D = 180$ K) exceeds the measured specific heat at 25 K, in the case of $\Theta_D = 210$ K the extrapolated anomalous entropy changes exceed the full magnetic entropy so that we conclude $\Theta_D = 195 \pm 25$ K. Figure 5(b) shows the associated magnetic entropy changes $\Delta S^{mag}(T)$ which have been obtained by integrating $\Delta c_p/T$, with $\Delta c_p = c_p\text{-}c_p^{ph}(\Theta_D = 195$ K). The resulting entropy changes agree with a vanishing field effect at $T \lesssim 7$ K. At $B = 0$, nearly 80% of the whole magnetic entropy changes $R\ln(2S + 1)$ are released below T_N which confirms a predominant three-dimensional (3D) nature of magnetic order in $MnSb_2O_6$ as found by neutron studies and DFT in Refs. [7,8]. In addition, as mentioned above, the data also imply residual magnetic entropy changes well above T_N.

For $B \leqslant 9$ T, there is no visible magnetic field effect on c_p at $T \lesssim 7$ K. The low-temperature behavior of c_p is approximately proportional to $T^{3/2}$. However, extrapolating the data implies that qualitative changes in the T dependence must be expected for $T < 2$ K. The observed low-temperature behavior $c_p \sim T^n$ with $n \approx 1.5$ contradicts the magnon specific heat expected in conventional 3D antiferromagnets, i.e., $n = 3$ while $n \sim 2$ is the behavior expected for quasi-two-dimensional (2D) antiferromagnets. Similar behavior is often found in frustrated spin systems [15]. E.g., the Kagomé-like jarosite $KCr_3(OH)_6(SO_4)_2$ shows $c_p \sim T^{1.6}$. The data are hence consistent with a frustrated spin system. The small hump in the specific-heat data of $MnSb_2O_6$ might, however, suggest an alternative interpretation as it may be associated with coupling of spin and dielectric degrees of freedom. In

magnetoelectric $LiFePO_4$, changes of the dielectric function below T_N are associated with a small hump of the specific heat which is reminiscent of the behavior observed in Fig. 5 [16,17].

IV. ELECTRON-SPIN RESONANCE

ESR spectra in Fig. 6 taken at $f = 260.5$ GHz show a single resonance line at high temperature which shifts and significantly broadens upon cooling. At $T = 250$ K, the data indicate a single ESR line associated with $g = 1.995 \pm 0.008$, which is common for high-spin Mn^{2+} in a paramagnetic phase. Upon cooling, the resonance fields shift as temperature approaches T_N, which is typically observed in AFMR spectra due to the evolution of internal fields. At $T = 2$ K, i.e., in the long-range spin-ordered state where HF-ESR is susceptible to collective magnon modes, a broad and asymmetric resonance feature is found which is typical for powder samples with magnetic anisotropy.

Accordingly, the low-temperature spectra are described by means of a powder model which involves different center resonance fields associated with the different orientations of the crystallites with respect to the external field. The simulation yields a good description of the spectra by means of an anisotropic effective resonance field ranging from a minimal resonance center field B_{res}^{min} to a maximal one B_{res}^{max} (see the inset in Fig. 8) [18]. Note that broadening due to an inhomogeneous effective field does not describe the spectra well.

Applying the powder spectra analysis described above allows us to study the temperature dependence of the resonance fields B_{res} in more detail. Figure 7 shows B_{res} as extracted from

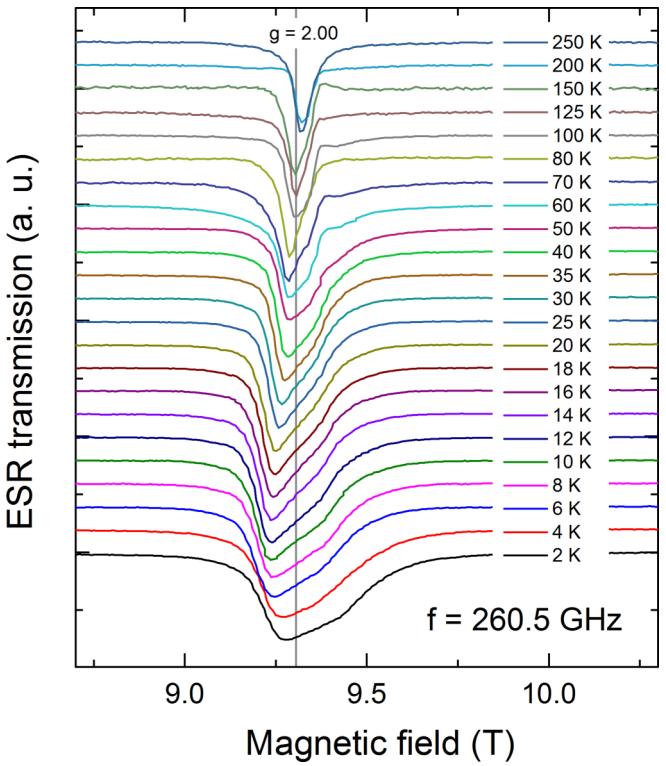

FIG. 6. Temperature dependence of HF-ESR spectra in the temperature range of 2 to 250 K, at $f = 260.5$ GHz.

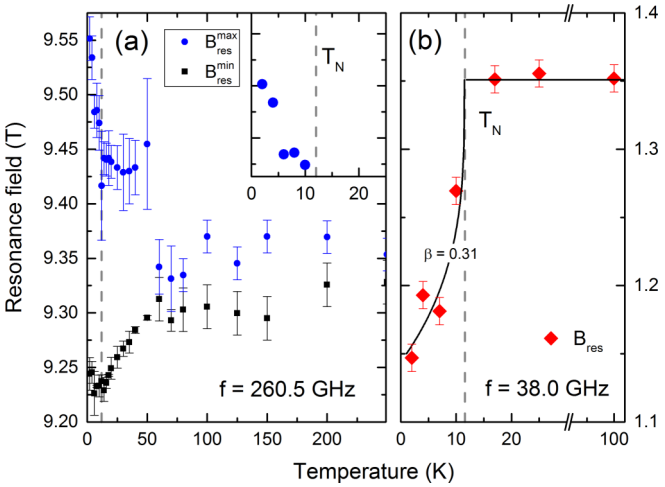

FIG. 7. (a) Temperature dependence of the HF-ESR resonance fields B_{res}, at 260.5 GHz. The resonance fields were obtained from powder spectra simulations. The inset magnifies the behavior upon crossing T_N. (b) B_{res} vs T obtained at 38.0 GHz where only one resonance field is observed. The line is a guide to the eye employing the critical exponent $\beta = 0.31$. Dashed vertical lines show T_N.

the data obtained at $f = 260.5$ and 38.0 GHz, respectively. At 38.0 GHz, the spectra are described by a single resonance field and there is no significant shift of B_{res} in the paramagnetic phase. A clear shift below T_N shows the evolution of an internal magnetic field in the long-range spin ordered phase, i.e., it reflects the magnetic order parameter. The evolution of long-range order below T_N is also seen at higher frequency $f = 260.5$ GHz where the broadened spectra are described by the resonance fields B_{res}^{max} and B_{res}^{min}, both of which shift when temperature crosses T_N. In contrast to the low-frequency data, the extracted resonance fields imply the evolution of internal magnetic field well above T_N, i.e., up to $T \sim 60$ K. Note that the original spectra in Fig. 6 indicate inhomogeneous broadening of the resonance even up to 150 K. Both observations imply the presence of internal magnetic field in the paramagnetic phase and hence the evolution of short-ranged magnetic order in this temperature regime. This result agrees with the observed deviation of the static magnetization data from the mean-field description below ~55 K (cf. Fig. 1) and magnetic entropy changes well above T_N (cf. Fig. 5).

Figure 8 summarizes the frequency dependence of the resonance fields, at $T = 4$ K. It comprises the resonance fields B_{res}^{max} and B_{res}^{min} derived by means of the analysis mentioned above. Note that the resonance feature associated with $\omega(B_{res}^{max})$ is less pronounced and is not observed at $f \leqslant 40$ GHz. For $f \geqslant 100$ GHz, both resonance branches $\omega(B_{res})$ exhibit a linear field dependence. This linear behavior at high fields implies the g factors $g_{res}^{min} = 2.008(3)$ and $g_{res}^{max} = 1.982(2)$. Below ~70 GHz, splitting between the two branches starts to increase and $f(B_{res}^{min})$ shows up-turn curvature indicative of finite zero-field splitting (ZFS).

A minimal model describing the observed AFMR modes applies a two-lattice system with easy-plane anisotropy. It is motivated by the cycloidal spin structure found in neutron diffraction in which due to large single-ion anisotropy spins are restricted to a plane including the c axis [7]. The resulting

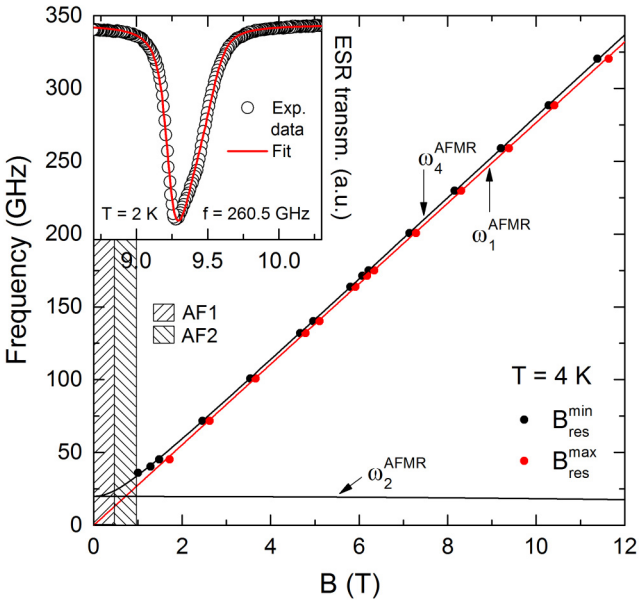

FIG. 8. Absorption frequencies-field diagram at $T = 4$ K. For each frequency, the resonance fields $B_{\rm res}^{\rm min}$ and $B_{\rm res}^{\rm max}$ have been derived by powder spectra simulations. Solid lines represent fits according to Eqs. (2)–(5) (see the text). Hatched areas refer to the phases AF1 and AF2 (cf. Fig. 4). Inset: HF-ESR spectrum at $f = 260.5$ GHz and $T = 2$ K. The line shows the simulated powder spectrum.

incommensurate spin order may be approximated by a 60° rotation of the spins in the xy plane. Note that the two-sublattice model agrees with the M versus B data while three sublattices are usually associated with additional features in the magnetization curves.

The corresponding minimal Hamiltonian reads

$$\mathcal{H} = -\mu_B \sum_j g\vec{S}_j\cdot\vec{H} - \sum_{ij} J_{ij}\vec{S}_i\cdot\vec{S}_j - D\sum_j \left(\vec{S}_j^z\right)^2. \quad (1)$$

Here, $\mu_{\rm B}$ is the Bohr magneton, g is the g value, D is the single ion anisotropy, and J_{ij} is the exchange coupling between spins $\vec{S}_i$ and $\vec{S}_j$. In the mean-field approximation and assuming $B_A \ll B_E$, higher orders of B_A can be neglected. B_A is the anisotropy field and B_E is the exchange field. The resulting AFMR modes read

$$\omega_1 = \gamma B, \quad (2)$$

$$\omega_2 = \gamma\sqrt{2B_AB_E - (B_A/2B_E)B^2} \quad (3)$$

for magnetic fields B in plane and

$$\omega_3 = 0, \quad (4)$$

$$\omega_4 = \gamma\sqrt{2B_AB_E - (1 - B_A/2B_E)B^2} \quad (5)$$

for magnetic fields B perpendicular to the plane, with γ the gyromagnetic ratio. Fitting of the experimental data by means of Eqs. (2) and (5) yields an anisotropy of $\sqrt{2B_AB_E} = 0.71 \pm 0.08$ T. The associated zero-field splitting amounts to 20 GHz. The fitted resonance branches ω_1 and ω_4 are shown in Fig. 8. Extracting the exchange field $B_E = B_C/2$ from the saturation field $B_C \approx 26$ T (cf. Fig. 4) allows us to estimate the planar anisotropy field $B_A = 0.02 \pm 0.01$ T. Note that this value refers to the two-sublattice model applied here. The resonances associated with the AFMR mode ω_2 are not observed and the shown branch has been calculated from the fitting parameter B_A and from B_E. According to the model, it becomes soft well above the field range shown in Fig. 7, i.e., at $2B_E = 26$ T.

LF-ESR data in the paramagnetic phase show a single exchange-narrowed Lorentzian line which is typical for a concentrated Mn^{2+} spin system. At $T = 300$ K in the paramagnetic regime, the average effective g factor amounts to $g = 1.995 \pm 0.001$ which is in perfect agreement with the HF-ESR data. While $B_{\rm res}$ and hence $g_{\rm eff}$ hardly shift upon cooling down to $T' \sim 35$ K, there is a pronounced increase of $g_{\rm eff}$ at $T_{\rm N} \leqslant T \leqslant T'$ K, which again signals short-range antiferromagnetic correlations. Consistently with the findings in HF-ESR, the LF-ESR signal vanishes below $T \sim T_{\rm N}$ because of the opening of the spin gap and the line broadening.

Perfect Lorentzian shape of the resonance line at 300 K rules out spin diffusion. Upon cooling, the linewidth ΔB continuously increases which may be due to critical behavior associated with the evolution of spin-spin correlations. The results are hence consistent with the presence of high-temperature antiferromagnetic correlations. Linewidth broadening can be described in terms of a power law of the reduced temperature, with the critical exponent p being associated with the spin dimensionality and the magnetic anisotropy of the system. With the temperature-independent linewidth $\Delta B(\infty)$ at infinite temperature, the critical slowing down is analyzed as follows:

$$\Delta B(T) - \Delta B(\infty) \propto A\left(\frac{T - T_{\rm N}}{T_{\rm N}}\right)^{-p} + B(T - T_{\rm N}). \quad (6)$$

The linear term ($B > 0$) is suggested by the data at $T \gtrsim 120$ K (see the inset of Fig. 9). Equation (6) appropriately describes $\Delta B(T)$ above $T \simeq T'$, with $p = 0.47(2)$ and $\Delta B(\infty) \approx 2$ mT (red line). Excluding the linear term yields $p = 0.32(1)$ (dashed blue line). Upon approaching $T_{\rm N}$, nonlinear behavior in the log plot implies failure of a power-law description. In terms of Eq. (6), the curved function would result in a continuous change of p below T'. The critical divergence becomes weaker upon approaching the 3D cycloidic spin ordered phase.

The observed critical exponent is much smaller than what is theoretically expected for 2D and 3D antiferromagnets [19] or what is found in one-dimensional antiferromagnets [20,21]. In contrast, it is similar to the behavior in the easy-plane magnet $CsMnF_3$ ($p = 0.51$) [22], in the 2D quantum antiferromagnet $SrCu_2(BO_3)_2$ ($p = 0.51$) [23], or in the 2D Ising antiferromagnet $MnTiO_3$ ($p = 0.49$) which is a linear magnetoelectric [24,25]. We also note similar behavior in triangular systems which are discussed in terms of the vicinity to a Berezinskii-Kosterlitz-Thouless (BKT) phase [26]. In general, the critical behavior found in $MnSb_2O_6$ is consistent with findings in systems with competing interactions.

Spin-lattice interaction may account for a (positive) linear-T contribution to ΔB as proposed for manganites in Ref. [27]. In these systems, an exchange narrowed line is considered

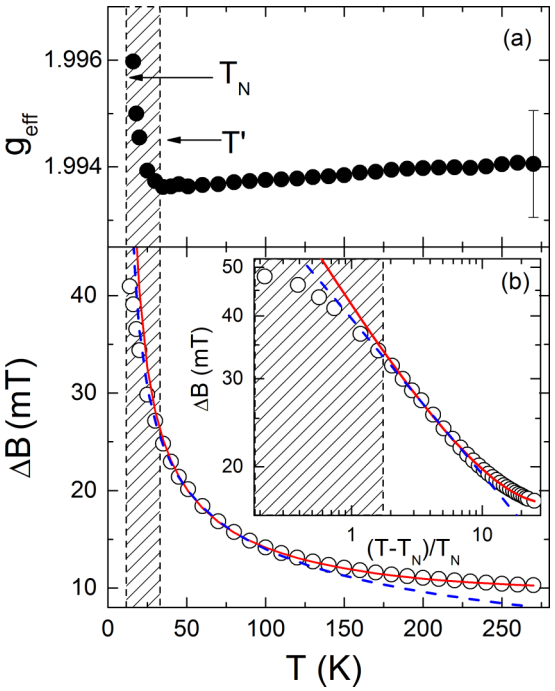

FIG. 9. (a) Effective g factor g_{eff} and (b) linewidth ΔB vs temperature derived from LF-ESR data. For $T' < T < 120$ K, $\Delta B(T)$ is well described by a power law [see Eq. (6)] (red and dashed blue line; see the text). The dashed area covers the temperature regime $T_N \leqslant T \leqslant T'$ where the power law fails to describe the data and where g_{eff} rapidly increases. At $T > 120$ K, the data either imply an additional linear term (red line) or indicate a second crossover regime (see the text). The error bar indicates the systematic uncertainty at room temperature.

where phonon modes with frequencies below a spin-spin relaxation rate contribute to the linewidth. Note, however, that a further change of the critical behavior towards $p \approx 0.17$ would describe the high-T behavior without employing an additional linear term. The strong increase of ESR linewidth with temperature found in $CuSb_2O_6$ can be ascribed to thermal activation of a dynamic Jahn-Teller effect [28] which is not present in the Mn^{2+} system at hand.

V. DISCUSSION

The HF-EPR data imply a small but finite planar anisotropy showing up in the zero-field splitting of the associated AFMR mode of approximately 20 GHz. Our analysis by means of an easy-plane two-sublattice model yields the anisotropy field $B_A = 0.02$ T which is in the typical range for Mn^{2+} ions. E.g., in $CaMnCl_3 \cdot H_2O$, B_A amounts to 0.06 T [29]. Our finding of the planar-type anisotropy qualitatively confirms the DFT results in Ref. [7], where, based on these band-structure calculations, Johnson *et al.* emphasize a crucial role of anisotropy for stabilizing the cycloidal spin structure in $MnSb_2O_6$ as it favors cycloidic over helical spin structure in the ground state. Our experimental data presented here, however, imply only very small anisotropy.

The presence of only small magnetic anisotropy is corroborated by the magnetic phase diagram which exhibits field induced phase transitions at low magnetic fields only. However, *two* field induced phase transitions are observed at $B_{C1} \approx 0.5$ T and $B_{C2} = 0.9$ T, respectively, at $T = 2$ K. Typically, small anisotropy yields conventional spin-flop transitions at moderate magnetic field as illustrated in $CaMnCl_3 \cdot H_2O$ at $B_{sf} = 1.6$ T [29]. Our analysis of the slope of the phase boundary (Fig. 4) indicates only small entropy differences between the associated antiferromagnetic phases AF2 and AF3. Following Ref. [7] one may speculate whether external magnetic fields affect the subtle interplay between the cycloidal spin structure, i.e., the ground state, and the helical one by tipping the energy balance towards the latter at B_{C1}, while B_{C2} may be associated with spin reorientation. The example of $BaCu_2Si_2O_7$ illustrates the possibility of a two-stage spin reorientation phenomenon. In this system, the relative arrangement of adjacent long-range antiferromagnetically ordered spins is hardly affected by external magnetic fields while the whole spin structure is reoriented in two phase transitions [30]. The AF3 phase probed by our HF-ESR and magnetization data at $B \gtrsim 1$ T is described neither with a three-sublattice model nor with six sublattices if magnetic coupling of magnitude reported in Ref. [7] for cycloidic order in AF1 is used. The fact that, in AF1 and AF2, no resonance is found, at $\geqslant 35$ GHz and at $B < 1$ T, suggests that AF1 and AF2 exhibit only small ZFS and hence small anisotropy, too, similar to the findings in AF3. A possible larger ZFS would show up in the HF-ESR data at $B < 1$ T and higher frequency. We, however, emphasize that the magnetic spectroscopies applied here do not discriminate between different spin structures as long as the associated AFMR modes can be described by means of a two-sublattice model. In addition, one may speculate whether the unusual temperature dependence of the specific heat, i.e., a field-independent humplike region in the ordered phase, is associated with the interplay of anisotropy and energetically neighboring states, too. Recently, it has come to our attention that the ground state at $B = 0$ was found to exhibit a small tilting from the (110) plane in the spin-spiral plane [31]. It is speculated that this tilting could arise from a small angle between the direction of the anisotropy and the [001] axis. We note that the HF-ESR data presented here probe the magnetic phase above 1 T.

Finally, our results imply short-range magnetic correlations well above T_N as consistently indicated by the shift of HF-ESR resonance fields below ~60 K, the failure of a power-law description in the LF-ESR data, and the observation of magnetic entropy changes at temperatures well above T_N. Such a wide range of antiferromagnetic fluctuations agrees with the structurally triangular, viz., magnetically frustrated arrangement of Mn^{2+} ions in $MnSb_2O_6$. The failure to describe the LF-ESR linewidth in terms of a single power law may indicate dimensional crossover when approaching the chiral magnetic ground state.

VI. SUMMARY

To summarize, we report the static and dynamic magnetic properties as well as specific heat of structurally and magnetically chiral $MnSb_2O_6$. The magnetic phase diagram shows

competing antiferromagnetic phases at small magnetic fields, i.e., at $B_{C1} \approx 0.5$ T and $B_{C2} = 0.9$ T. The AFMR modes imply planar anisotropy which qualitatively confirms recent predictions [7]. The data are well described by means of an easy-plane two-sublattice model with the anisotropy field $B_A = 0.02$ T. The exchange field $2B_E = 26$ T is obtained from the saturation field of the static magnetization. The results are discussed in terms of a delicate balance of cycloidal and helical spin structures under the influence of small planar anisotropy and external magnetic field. The frustrated nature of the system is reflected by the fact that short-range magnetic correlations are observed well above T_N.

ACKNOWLEDGMENTS

We are very grateful to V. B. Nalbandyan and A. Yu. Nikulin for providing the sample for this study. J.W., R.K., and E.A.Z. acknowledge financial support by the Excellence Initiative of the German Federal Government and States. E.A.Z. appreciates support from the Russian Foundation for Basic Research (Grant No. 14-02-00245). This work was supported in part by the Ministry of Education and Science of the Russian Federation in the framework of Increase Competitiveness Program of NUST "MISiS" (Grant No. K2-2015-075) and by Act 211 Government of the Russian Federation, Contract No. 02.A03.21.0006.

[1] T. Lottermoser, T. Lonkai, U. Amann, D. Hohlwein, J. Ihringer, and M. Fiebig, Nature (London) **430**, 541 (2004).

[2] W. Eerenstein, N. D. Mathur, and J. F. Scott, Nature (London) **442**, 759 (2006).

[3] S. W. Cheong and M. Mostovoy, Nat. Mater. **6**, 13 (2007).

[4] M. Fiebig, J. Phys. D **38**, R123 (2005).

[5] J. Wang, J. B. Neaton, H. Zheng, V. Nagarajan, S. B. Ogale, B. Liu, D. Viehland, V. Vaithyanathan, D. G. Schlom, U. V. Waghmare, N. A. Spaldin, K. M. Rabe, M. Wuttig, and R. Ramesh, Science **299**, 1719 (2003).

[6] M. Matsuda, R. S. Fishman, T. Hong, C. H. Lee, T. Ushiyama, Y. Yanagisawa, Y. Tomioka, and T. Ito, Phys. Rev. Lett. **109**, 067205 (2012).

[7] R. D. Johnson, K. Cao, L. C. Chapon, F. Fabrizi, N. Perks, P. Manuel, J. J. Yang, Y. S. Oh, S.-W. Cheong, and P. G. Radaelli, Phys. Rev. Lett. **111**, 017202 (2013).

[8] J. N. Reimers, J. E. Greedan, and M. A. Subramanian, J. Solid State Chem. **79**, 263 (1989).

[9] V. B. Nalbandyan, E. A. Zvereva, A. Y. Nikulin, I. L. Shukaev, M. H. Whangbo, H. J. Koo, M. Abdel-Hafiez, X. J. Chen, C. Koo, A. N. Vasiliev, and R. Klingeler, Inorganic Chemistry **54**, 1705 (2015).

[10] H. G. Scott, J. Sol. State. Chem. **66**, 171 (1987).

[11] P. Comba, M. Großhauser, R. Klingeler, C. Koo, Y. Lan, D. Müller, J. Park, A. Powell, M. J. Riley, and H. Wadepohl, Inorg. Chem. **54**, 11247 (2015).

[12] M. E. Fisher, Phil. Mag. **7**, 1731 (1962).

[13] A. Tari, *The Specific Heat of Matter at Low Temperatures* (Imperial College, London, 2003).

[14] S.-L. Drechsler, O. Volkova, A. N. Vasiliev, N. Tristan, J. Richter, M. Schmitt, H. Rosner, J. Malek, R. Klingeler, A. A. Zvyagin, and B. Büchner, Phys. Rev. Lett. **98**, 077202 (2007).

[15] A. P. Ramirez, Annu. Rev. Mater. Sci. **24**, 453 (1994).

[16] C. Neef, Ph.D. thesis, Heidelberg University, 2016.

[17] R. Toft-Petersen, M. Reehuis, T. B. S. Jensen, N. H. Andersen, J. Li, M. D. Le, M. Laver, C. Niedermayer, B. Klemke, K. Lefmann, and D. Vaknin, Phys. Rev. B **92**, 024404 (2015).

[18] S. Stoll and A. Schweiger, J. Magnetic Resonance **178**, 42 (2006)

[19] H. Benner and J. P. Boucher, in *Magnetic Properties of Layered Transition Metal Compounds*, edited by L. J. de Jongh (Kluwer Academic, Dordrecht, 1990), pp. 323–378.

[20] A. F. M. Arts, H. van der Vlist, J. G. M. van Miltenburg, C. M. J. van Uijen, and H. W. de Wijn, J Magn. Magn. Mat. **31–34**, 1181 (1983).

[21] Y. Ajiro, S. Matsukawa, T. Yamada, and T. Haseda, J. Phys. Soc. Jpn. **39**, 259 (1975).

[22] G. L. Witt, Physica **61**, 476 (1972).

[23] A. Zorko, D. Arcon, A. Lappas, and J. Giapintzakis, Phys. Rev. B **65**, 024417 (2001).

[24] J. Akimitsu and Y. Ishikawa, J. Phys. Soc. Jpn. **42**, 462 (1977).

[25] N. Mufti, G. R. Blake, M. Mostovoy, S. Riyadi, A. A. Nugroho, and T. T. M. Palstra, Phys. Rev. B **83**, 104416 (2011).

[26] Y. Ajiro, H. Kikuchi, S. Sugiyama, T. Nakashima, S. Samoto, N. Nakayama, M. Kiyama, N. Yamamoto, and Y. Oka, J. Phys. Soc. Jpn. **57**, 2268 (1988).

[27] D. L. Huber, arXiv:1309.6353.

[28] M. Heinrich, H.-A. Krug von Nidda, A. Krimmel, A. Loidl, R. M. Eremina, A. D. Ineev, B. I. Kochelaev, A. V. Prokofiev, and W. Assmus, Phys. Rev. B **67**, 224418 (2003).

[29] A. C. Phaff, C. H. W. Swüste, K. Kopinga, and W. J. M. de Jonge, J. Phys. C **16**, 6635 (1983).

[30] A. Zheludev, E. Ressouche, I. Tsukada, T. Masuda, and K. Uchinokura, Phys. Rev. B. **65**, 174416 (2002).

[31] M. Kinoshita, S. Seki, T. J. Sato, Y. Nambu, T. Hong, M. Matsuda, H. B. Cao, S. Ishiwata, and Y. Tokura, Phys. Rev. Lett. **117**, 047201 (2016).